2026 IEEE International Conference on Robotics and Automation (ICRA 2026)
June 1-5, 2026. Vienna, Austria

Puzzle Piece Robots: Inverse-Designed Shape-Morphing Docking for Spherically Reconfigurable Soft Robots

Justin Conzola and Vishesh Vikas[1]

***Abstract*—Modularity in robots enhances versatility, enabling shape morphing and reconfiguration. In modular soft robots, the use of soft materials allows dimensional transformations across different architectures - from chains (1D) to lattices (2D) and spheres (3D). All this enables a swarm of robots to exhibit multi-modal locomotion - such as millipede-like, starfish-like, and soccer-ball-like movement patterns. However, achieving such reconfiguration remains challenging, especially in soft robots, where docking is difficult to realize without compromising compliance. Conventional approaches - such as rigid inserts, magnetic actuators, and adhesives - face challenges due to rigid–soft fabrication mismatch, interference with body compliance and limited holding strength. To address these challenges, this work proposes a geometric, active shape-morphing docking mechanism for spherically reconfigurable soft robots, that combines concepts of topology design and mechanical metamaterials. The robot module edges are designed to create geometric interlocks between adjacent edges (similar to jigsaw puzzle pieces) with an internal structure that deforms under actuation by inlaid shape memory alloy (SMA) wires. The metamaterial internal structure is obtained through inverse design optimization of a computational deformation model created in Abaqus CAE. The constraint-aware optimization strategy blends random search and genetic algorithm features to handle a large number of bounded variables and nonlinear objective function, driving convergence toward a global minimum via geometric decay of the search space. The resulting optimal geometry is designed to buckle under high localized forces, enabling docking and undocking, while remaining minimally deformed under distributed forces, thereby passively maintaining coupling during operation. The docking mechanism is experimentally validated by confirming that the deformation achieved under actuation can facilitate the docking operation and through locomotive testing where two docked modules completed 120 locomotive actuation cycles without disconnecting.**

***Index Terms*—soft robots, inverse design, reconfigurable robots, docking mechanism, metamaterial, modular robots**

I. Introduction

Navigation of unstructured terrain remains one of the central challenges in field robotics. From search and rescue operations and agricultural monitoring to extraterrestrial planetary exploration, bringing robots out of the lab and into the field requires robust autonomous systems capable of addressing complex locomotion challenges. Modular, reconfigurable robots address this by forming complex configurations that enhance environmental interaction and even enable obstacle avoidance. Modular Soft Robots (MSoRos), in turn, have proven to further enhance the versatility and scalability that modular robots aim to achieve. High compliance allows them to deform and conform to the environment, enabling multi-dimensional reconfiguration into millipede-like chain (1D), starfish-like lattice (2D) and soccer-ball-like sphere (3D) [1]. Here, a swarm of MSoRos can work collectively to alter locomotion modes, e.g., reconfigure into a chain to bypass large obstacles, a sphere to exhibit energy-efficient, fast rolling, or separate into lattice to explore the environment. A robust coupling method is central to realizing the full potential of modular robots. These docking systems require high holding forces to maintain coupling during operation while being compliant enough to allow the modules to reach their entire configuration space and account for misalignment between modules during the coupling process. Docking in spherically reconfigurable robots is particularly challenging because the docking interface must operate reliably in two distinct geometric states: a flat configuration and a deformed spherical configuration. This implies that the coupling method itself should be flexible [2].

Traditional modular robots employ mechanical connection mechanisms - including pin-and-hole systems [3]–[8], hooks and clamps [9]–[15], and shape-matching interfaces [16], [17] - or magnetic connections using permanent magnets [18]–[23] or electromagnets [24]–[26]. Some soft modular robots also utilize these traditional coupling methods. For example, Zhang et al. embedded permanent magnets within rigid connecting parts on the ends of soft actuators [27]. Robot modules are released by inflating a pneumatic bladder to physically separate them. Others [28], [29] use similar permanent magnet docking methods in their soft robots. Although these robots have been successful in their respective applications, their reliance on pneumatics for both locomotion and decoupling results in limited potential for untethered deployment outside of lab environments. Additionally, the introduction of rigid magnets to the soft robots interferes with their compliance. Mechanical coupling strategies for soft robots have also been researched. Perhaps the most unique docking mechanism in the literature comes from Malley et al. [30]. Their approach uses a corkscrew mechanism which allows robot modules to dock with each other at any point on the body rather than at discrete points, allowing them to build complex structures. Another work used permanent mechanical connectors for modular worm-like soft robots connected in series [31].

Outside of these traditional coupling methods, researchers

*This work is supported in part by the National Science Foundation (NSF) under Award #1830432, and USFA/NIFA Award #2023-67022-40918

[1]Justin Conzola and Vishesh Vikas are with the Agile Robotics Lab (ARL), University of Alabama, Tuscaloosa AL 35487, USA (e-mail: jhconzola@crimson.ua.edu; vvikas@ua.edu).

have explored additional strategies that take advantage of light weight and versatility of soft materials to avoid the continuum disruptions caused by traditional docking mechanisms. Materials that exhibit viscoelastic behavior at room temperature and transition to thermoplastics when heated have been used to make reversible adhesive connections between robot modules [32], [33]. This approach results in high relative holding forces at the cost of long docking cycles. Yang et al. developed a thermoplastic foam to this end which can withstand forces up to $6.84\,\mathrm{N/cm^2}$ contact area, but requires 2 minutes to heat into a thermoplastic state and another 9 minutes to cure during module attachment. Germann et al. [34] proposed a docking strategy for lightweight pneumatic robots using electrostatic adhesion. This method is limited to ultra lightweight robots, due to the low nominal holding forces.

Contributions: This work proposes a soft mechanical docking mechanism for spherically reconfigurable soft robots where the module edges interlock like jigsaw puzzle pieces. The topology design methodology includes (1) generation of a novel module edge topology with geometric interlocks between adjacent modules, using an analytical approach involving inverse orthographic and azimuthal projections, that assist with docking in planar and spherical configuration; (2) inverse-design optimization of a cell-based mechanical metamaterial array using a high-fidelity quasi-static computational model for the deformation of the mechanism under loading conditions and optimization of the array cell dimensions by a custom constraint-aware random search algorithm. The resulting optimal geometry buckles under high localized forces, allowing for docking and undocking operations to be performed, but is only subjected to minimal deformation by distributed forces, allowing it to passively maintain coupling during operation. The overall design flow can be seen in Fig. 1. The computational model is experimentally validated by the displacements of key points and the efficacy of the docking mechanism is validated by deformation testing and locomotive experiments with docked modules.

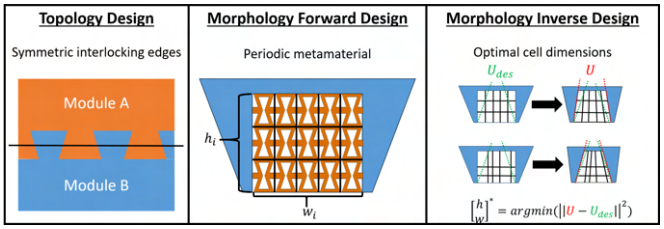

Fig. 1: Design flow for geometric docking: Module topology is defined such that module edges allow interlocking, similar to how jigsaw puzzle pieces fit together. A periodic metamaterial array is inlaid in the "male" portions of the interlocks to accommodate deformation under loading. The cell dimensions of the metamaterial array are optimized to minimize the distance between the true and desired deformations.

II. Topology Design

The topology design concept for the docking mechanism centers around generating module edges that interlock like pieces in a jigsaw puzzle, so that once connected, large deformation is required to decouple. These geometric interlocks provide a unique embodied solution to the docking problem. This section provides a brief review of a previously established polyhedra-based method for generating spherically reconfigurable MSoRo topology and then defines a new family of module topology curves (MT curves) with geometric interlocking.

A. Brief Overview of Topology Design

Topology of soft robot modules capable of achieving a spherical configuration are generated using an established framework. The method, outlined in Fig. 2, uses a base platonic or Archimedean solid to determine the number of robot modules in the set and the number of limbs on each robot. An MT curve is an odd function that determines the overall limb and module topology. This curve is sketched in a plane containing the target edge, oriented orthogonal to the vector between the base solid center and the target edge center. A series of projections are then used to generate robot topology in spherical and planar configurations. For more information on module topology generation, the reader may refer to [1], [35].

B. Self-Locking Module Topology

The MT curves are constrained to be odd functions to ensure that they coincide at the vertices of the base polyhedron. Previous works have considered continuous sinusoidal MT curve function family; however, the creation of geometric locks in the topology requires that the topology curve "doubles back" on itself and hence must be either a piecewise or parametric function. The selected parametric MT curve, referred to as the "Jigsaw MT curve", begins and ends with a quarter sine wave of frequency $2a$ where a being edge length of the base polyhedron, and the central portion is a rotation of the parametrically defined interlocking geometry.

$$f(x) = \begin{cases} -\frac{Aa}{2}\sin(\frac{4\pi x}{a}) & -\frac{a}{2} < x < -\frac{3a}{8} \\ F_d(x, A, a, C, n, \theta) & -\frac{3a}{8} < x < -\frac{3a}{8} \\ -\frac{Aa}{2}\sin(\frac{4\pi x}{a}) & \frac{3a}{8} < x < \frac{a}{2} \end{cases} \quad (1)$$

where F_d is the parametric docking function and $A \in [0, 1]$ is the relative amplitude of the sine wave. C, θ, n are the height, inclination angle and number of the geometric interlocks respectively, as visualized in Fig. 3. F_d is developed in a separate plane which uses coordinates (x_r, y_r). The relationship between the (x, y) and (x_r, y_r) coordinate systems is a planar rotation about the edge center by angle ϕ

$$\begin{bmatrix} x \\ y \end{bmatrix} = \begin{bmatrix} \cos(\phi) & -\sin(\phi) \\ \sin(\phi) & \cos(\phi) \end{bmatrix} \begin{bmatrix} x_r \\ y_r \end{bmatrix} \quad (2)$$

where $\phi = \mathrm{atan2}(\frac{A}{2}, \frac{3}{8})$. The domain of the docking function is $x_r \in [-\frac{l}{2}, \frac{l}{2}]$ and $l = a\sqrt{(A-C)^2 + \frac{9}{16}}$. The domain

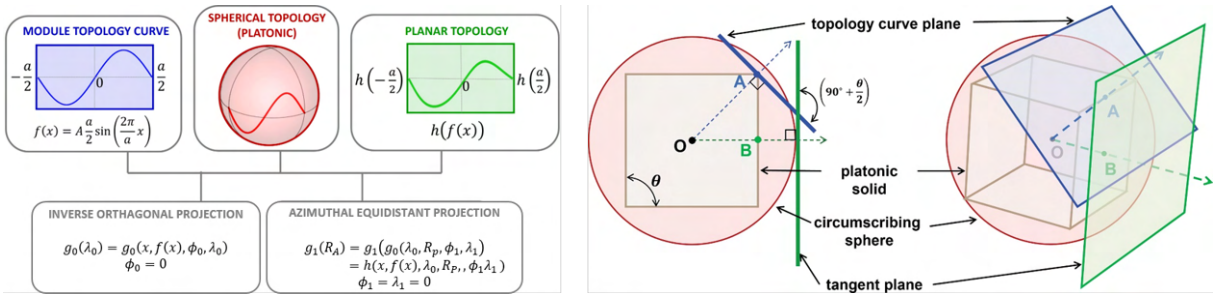

Fig. 2: (left) Summary of the topology design method involving orthographic projection onto a sphere and azimuthal equidistant projection onto a plane. (right) Visualization of the projection planes relative to the base solid and circumscribing sphere [1]

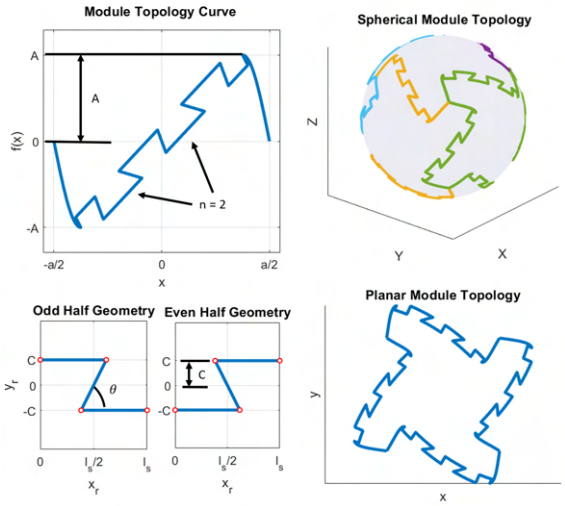

Fig. 3: (left) The generated module topology curve - an odd-function with geometric interlocks. Critical points from Tab. I are marked in red and topology parameters A, C, θ, n are labeled. (right top) spherical and (right bottom) planar robot module topology

is then segmented into $2n+1$ portions where mirror-image "half-locks", which can be seen at the bottom of Fig. 3 are alternated such that $p_{4,i-1} = p_{1,i}$. Each half-lock is defined by critical points and the remaining points linearly interpolated. The x_r coordinates of each half lock are identical and are a function of lock parameters: length $l_s = \frac{l}{2n+1}$, angle θ, and height C.

$$x_r^{1,i} = -\frac{l}{2} + l_s(i-1), \quad x_r^{2,i} = x_r^{1,i} + \frac{l_s}{2} + C\cot(\theta),$$
$$x_r^{3,i} = x_r^{2,i} - C\cot(\theta), \quad x_r^{4,i} = -\frac{l}{2} + l_s i \tag{3}$$

The y_r value corresponding to each x_r value will be $\pm C$. As mirror images, $y_r^{k,i} = -y_r^{k,i\pm1}$. This guarantees that the endpoints of each half lock will coincide with each other. The full set of y_r coordinates corresponding to each x_r for odd and even i are provided in Tab. I. The full MT curve is shown in Fig. 3 along with renderings of the module spherical and planar topologies.

TABLE I: y_r values for each x_r in the even and odd half locks.

x-Coordinate	Odd	Even	x-Coordinate	Odd	Even
x_r^1	$+C$	$-C$	x_r^2	$+C$	$-C$
x_r^3	$-C$	$+C$	x_r^4	$-C$	$+C$

III. Docking Mechanism Design

To accommodate the docking and undocking process, a reversible mechanism that collapses under actuation and recovers upon release is designed. This is achieved by incorporating an auxetic metamaterial pattern within the male locking geometry of the topology. A 3×5 array of cells with each row and column having unique heights and widths creates 15 unique cellular structures, defined by only 8 variables. Actuation is performed using shape memory alloy (SMA) coils routed through the structure. This section discusses the forward design of the internal structure and inverse design using a simulation framework in Abaqus CAE.

A. Forward Design of the Buckling Structure

A re-entrant honeycomb cell is selected as the base structure for the shape morphing mechanism as it is known to exhibit both auxetic and syncalastic behavior [36]. Synclasticity is of particular importance here for achieving spherical reconfiguration of the module set. The 3×5 array of cells with equal heights and widths are shown in Fig. 4. The pattern is placed within a rectangle that ensures enough shell thickness to store sufficient energy to return the geometry to the undeformed state when released. Additional design constraints require that the beams of the shell elements be at least $0.85\,\mathrm{mm}$ thick due to manufacturing limitations, and corresponding minimum height and width dimensions of $3.5\,\mathrm{mm}$ ensure that there are no conflicts generating the pattern.

B. Simulation Setup

A high-fidelity numerical model is developed to simulate the deformation of the docking mechanism. The docking

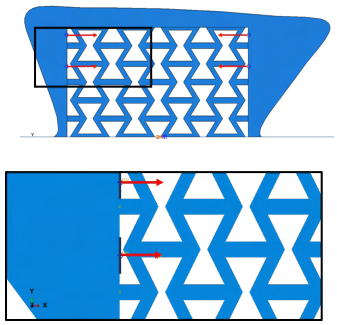

Fig. 4: The actuator assembly simulation with loads and boundary conditions. Red arrows indicate loads, applied to rigid shells tied to the soft body

geometry is isolated, with the remainder of the limb being represented as a fixed rigid surface. Additionally, the use of a planar auxetic structure allows the model to be reduced to 2D which greatly reduces simulation times. Analysis is performed in a Dynamic Explicit step with a slow loading rate in order to maintain the quasi-static condition. Mass scaling was used to ensure the solver operated at a desired time increment, and adaptive re-meshing ensured the simulation would not fail at large deformations. The assembled actuator with boundary conditions and applied loads is shown in Fig. 4.

Interactions: The simulation includes seven bodies: the rigid surface mentioned above, four additional rigid surfaces where loads are applied, an outer shell capturing the topology and a metamaterial lattice. The outer shell and lattice are both modeled as deformable shells. The decision to separate the outer shell from the lattice was made based on ease of use in the Abaqus-Python Interface (API) and to ensure a well-structured mesh. Tie constraints are applied at all edges where the bodies intersect making the model numerically equivalent to having all bodies in the same part. A general contact interaction is applied to the entire body with hard contact in the normal direction, to prevent bodies from overlapping, and high friction ($\mu = 1.0$) in the tangential direction.

Material and Section Assignments: Each of the two shell bodies are applied a homogeneous material section of Dragonskin 10A Medium Cure by Smooth On™ which uses a first order Neo-Hookean hyperelastic model. Hyperelastic parameters were obtained from the Soft Robotics Material Database [37] and density from product data sheet. Relevant material data is given in Table II.

Loading and Boundary Conditions: The forces applied by the SMA wires are simulated as point loads on the small rigid wires tied to the outer shell part. The force magnitude was determined from experimental analysis of the SMA coils used in the actuator. The manufacturer recommends pre-straining the wires by 150% to maximize force output and prevent plastic deformation of the wire. Experiments were carried out to characterize the force production at varying current levels. The results indicated an approximately linear relationship between current and force generation, i.e, $F = 0.18 \times (\text{current}) \times (\text{SMA free length})$. Undeformed wire lengths were determined by measuring the width of the mechanism at the actuation height on the CAD model, and the current divider law was used to estimate the portion of the overall current that would pass through each wire. The loads were gradually applied in smooth step over the length of the simulation. A fully encastrated boundary condition was applied to the reference point of the rigid ground part and the rotational degree of freedom was constrained on the rigid bodies where the loads are applied to ensure the directionality of the SMA forces remained accurate throughout the simulation step.

TABLE II: Material and Metamaterial Array Parameters

Category	Parameter	Symbol	Value
Material Parameters	Density	ρ	$1.07\,\mathrm{g\,cm^{-3}}$
	Initial Shear Modulus	C_{10}	$0.0778\,\mathrm{MPa}$
	Material Incompressibility	D_1	0.0
	Self Contact Friction	μ	1.0
Metamaterial Array Parameters	Total Height	H	$15\,\mathrm{mm}$
	Total Length	L	$25\,\mathrm{mm}$
	Rows	–	3
	Columns	–	5
	Beam Thickness	t	$0.85\,\mathrm{mm}$

C. Inverse Design of Buckling Geometry

The forward simulation is parameterized and automated using the API so that it can be looped during the optimization process. The heights and widths of each cell serve as the design variables in the minimization problem. A target boundary for the outer shell, an edge angle of 90° on both sides, is considered to be ideal as it provides acceptable clearance for the module edges to interlock. The objective function is evaluated at the connection interface between the inner and outer shell components. The desired x-axis displacement of each node is determined by the undeformed y-coordinate h_i and the undeformed edge angle θ_j as $u_{des,i} = h_i \cot\theta_j$. Simulated x-axis displacements of the nodes u_i are extracted from the last frame of the simulation. The overall objective function for obtaining the optimal cell pattern is defined as

$$X^* = \arg\min \left(\sum_i (u_{i,des} - u_i)^2 \right) \tag{4}$$

where X are constrained with upper and lower bounds to reflect manufacturing capabilities and prevent the creation of unstable cells that would drastically increase simulation times. Each horizontal and vertical cell dimension were subjected to the same bounds (w_l, w_u) and (h_l, h_u), respectively.

The full constraint equation is

$$\underbrace{\begin{bmatrix} 1^T & 0 & 0 & 0 & 0 & 0 \\ 0 & 1^T & 0 & 0 & 0 & 0 \\ I & 0 & I & 0 & 0 & 0 \\ 0 & I & 0 & I & 0 & 0 \\ I & 0 & 0 & 0 & -I & 0 \\ 0 & I & 0 & 0 & 0 & -I \end{bmatrix}}_{A} \underbrace{\begin{bmatrix} h \\ l \\ s_{hu} \\ s_{wu} \\ s_{hl} \\ s_{wl} \end{bmatrix}}_{X} = \underbrace{\begin{bmatrix} H \\ W \\ h_u \\ w_u \\ h_l \\ w_l \end{bmatrix}}_{b} \tag{5}$$

A custom global optimization strategy was employed to minimize the objective function. This approach was chosen due to two factors: (1) the large number of design variables with wide bounds necessitates an exploratory method, and (2) the high degree of nonlinearity and quasi-static kinematic model result in a non-smooth, non-convex objective function. The strategy borrows attributes from random search and genetic algorithms, but is fully constraint aware and ensures convergence to a global minimum through geometric decay of the search area. Points are generated by performing random pivots, accepted by the constraints, until a target distance from the parent point is reached. The initial point is calculated as $X_0 = A^{\dagger}b$ where $A^{\dagger}$ is the pseudo-inverse of A, and an initial search radius is calculated as $r_0 = \max(\sqrt{(X - X_0)^T(X - X_0)})$, s.t. $AX = b, X \geq 0$ to ensure that all feasible solutions are reachable. All children in generation 1 use X_0 as a parent and are randomly pivoted to a target distance $r \leq r_0$. In each subsequent generation, an even number of children use each of the previous generation's survivors as a parent and have a search radius from their parent of $r \leq r_0\varphi^{-(i-1)}$ for the i^{th} generation, where $\varphi = \frac{1+\sqrt{5}}{2}$ (the golden ratio). 4 generations with 64 children per generation were tested for a total of 256 points in each optimization. The pseudo-code for the optimization algorithm can be found in the Appendix.

IV. Results and Discussion

This section presents and discusses the optimal designs for both male docking segments. The simulation is validated by comparing the docking edge angles between the simulated results and the real fabricated system. The effectiveness of the docking is evaluated by performing multi-module planar locomotion.

A. Model Validation

The deformation model was validated experimentally prior to performing the optimization. The initial case of the upper docking geometry ($X = A^{\dagger}b$) was fabricated as a standalone actuator. The points used in the objective function were marked with small ink dots (marked in red in Fig. 5 (a)) on the surface and a camera was positioned so that the actuator was axially aligned in the frame. A full actuation cycle of the deformation and recovery of the actuator was recorded and static images of both the undeformed and deformed states were extracted for processing. The average displacement error across the 6 points was $0.2949\,\mathrm{mm}$ which is marginal relative to the overall lattice width of $25\,\mathrm{mm}$. Most of the error can be attributed to manufacturing defects. The mold for casting the test specimen was 3D printed using an FDM printer with a $0.4\,\mathrm{mm}$ nozzle. After analyzing the specimen, it was found that the beam thickness of the metamaterial lattice was $0.1\,\mathrm{mm}$ larger than anticipated. This was corrected in the simulated model for all versions, however it is probable that there are also slight differences in the outer shell thickness contributing to the errors. Additionally, small inconsistencies in the lengths of the SMA wires will impact the average forces generated at each loading position. Despite these two issues, the dominant behavior of the outer shell is preserved, as seen in Fig. 5 (b). Based on this analysis, the authors determined the model to be satisfactory for use in the optimization framework.

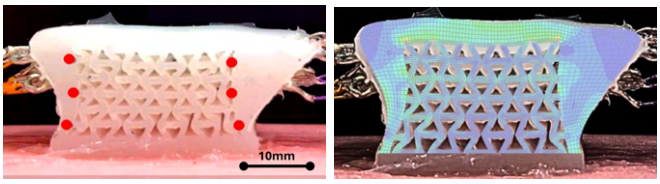

(a) (b)

Fig. 5: (a) The experimental setup for capturing the displacements of select nodes. Markers for the points of interest are marked in red. (b) The deformed mesh from the simulation overlayed on the experimental results.

B. Optimal Designs

The optimizer quickly converges to an optimal solution. Figure 6 plots the best solution in each generation, showing that the upper position converges in the first three generations and the lower position in the first two. The optimized cellular structures for each docking position are shown in Fig. 7. The right side of the figure shows the deformed state of each docking position relative to the target boundaries from the optimization problem. The minimum clearance for the docking operation requires that the minimum width of the female portion of the interlocking geometry be larger than the maximum width of corresponding male portion in the deformed state. The widths of the male geometry portions were extracted directly from the simulation file and the deformed gap widths were estimated as

$$w_{def} = w_{undef} + ||u_{adj}|| \tag{6}$$

where u_{adj} is the sum of the x-displacement of furthest point from the center at each edge adjacent to the female position. The dock between the upper male portion and the lower female portion had a minimum clearance of $1.3\,\mathrm{mm}$ and the dock between the lower male portion and upper female portion had minimum clearance of $4.9\,\mathrm{mm}$. Deformation tests of a physical model were performed to verify the simulated results. The supporting video submission provides a visual demonstration of the validation of results.

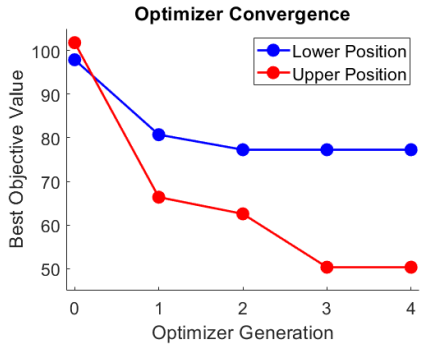

Fig. 6: Convergence of the optimization procedure, showing the best objective function value in each generation

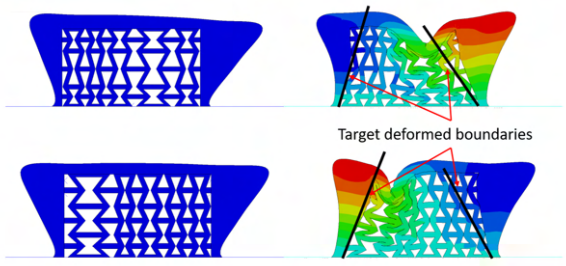

Fig. 7: Simulated results for the deformation of the docking mechanism. The left side shows the undeformed state and the right plots the deformed mechanism.

C. *Locomotive Testing for Passing Docking Strength Analysis*

Two full robot modules were fabricated and manually docked so that locomotive testing could be performed. 120 cycles of a rotation gait, where the free limbs are actuated and the docked limbs are left stationary, were performed to test the effectiveness of the docking mechanism's passive holding strength. Fig. 8 shows the state of the connection prior to and after the execution of the gait cycle. Over the course of the 120 gait cycles, the outer docking positions slipped about halfway and the inner docking positions remained fully connected. This validated the effectiveness of the mechanism when the robots are working collectively. The same gait cycle was executed again, but with only one of the modules actuated to test the docking strength under higher stress. Across 3 trials, a single outer position was broken each time after an average of 32 cycles. However, the other 3 positions remained docked further supporting the robustness of this mechanism by its ability to function after partial failure (Fig. 9).

V. Conclusion

This work outlines the design of a soft mechanical docking mechanism for modular soft robots. A curve to define module edge topology with geometric interlocks was generated within the constraints of a previously established design framework. The male portions of the interlocking geometry were transformed into a deformable docking mechanism

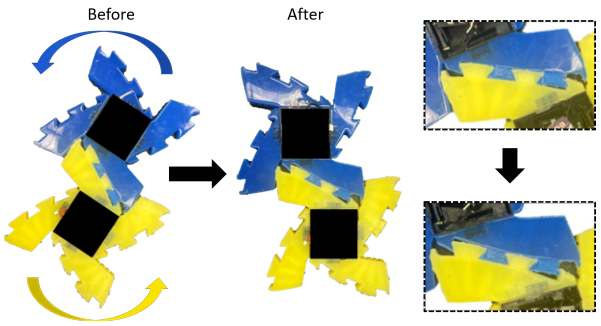

Fig. 8: 120 cycles of a locomotive gait were performed with two robot modules docked. The docking mechanism held with only minimal slippage, marked on the modules.

by placing an auxetic metamaterial array within them and routing SMA wires through the structure. A numerical model for predicting the deformation of the docking mechanism was developed using Abaqus CAE and experimentally validated. Finally, a custom constraint-aware global optimization strategy, which borrows attributes from random search and genetic algorithms and ensures convergence through geometric decay, was implemented to optimize the parameters of the metamaterial array. The efficacy of the docking mechanism was validated using two methods. Deformation testing ensured that the mechanism achieves sufficient edge displacement to provide clearance for the coupling action, and locomotive testing demonstrated the passive holding strength of the mechanism during operation, including continued functionality after partial failure. Experimental deformation test results suggest a high sensitivity to manufacturing defects, particularly evident in the reversed buckling direction along the top edge of the upper docking position (see supporting video). Further inspection of the mechanism revealed that the SMA wires exit and reenter the routing channels in certain locations leading to these unexpected changes in buckling behavior. Future efforts will aim to improve the manufacturing repeatability by inlaying the SMA wires within the silicone matrix during the casting process rather than routing them through channels afterwards and containing all wiring to within the silicone body. This move towards system-level integration plays a crucial role in the realization of multi-module locomotion in field operations. Planned works include gait synthesis for various multi-module configurations, autonomous seeking and docking, and 3D spherical reconfiguration of the modular system.

Appendix

References

[1] C. Freeman, M. Maynard, and V. Vikas, "Topology and morphology design of spherically reconfigurable homogeneous modular soft robots," *Soft Robotics*, vol. 10, no. 1, pp. 52–65, 2023.

[2] C. Zhang, P. Zhu, Y. Lin, Z. Jiao, and J. Zou, "Modular soft robotics: Modular units, connection mechanisms, and applications," *Advanced Intelligent Systems*, vol. 2, no. 6, p. 1900166, 2020.

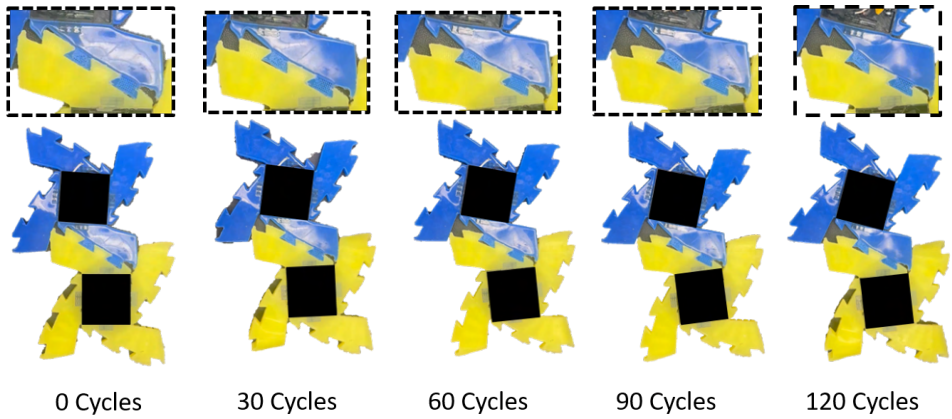

Fig. 9: An additional test with only one module actuated maximized the force exerted on the docking mechanism. Only one of four docked positions failed during this test.

Algorithm 1 Multi-Generation Random Search with Radius Decay

Require: Constraint matrix $\mathbf{A}$, constraint vector $\mathbf{b}$
Require: Population size N_{pop}, generations G, points per generation N_{gen}, max pivots K_{max}
Ensure: Optimal solution $\mathbf{x}^*$ and objective value f^*
Initialize $\phi^{-1} = \frac{2}{1+\sqrt{5}} \approx 0.618$ {Inverse golden ratio}
Initialize $\mathbf{X}_0 \leftarrow \mathbf{A}^\dagger \mathbf{b}$ {Initial feasible solution}
Extract $\mathbf{X}_0 = [\mathbf{x}_0, \mathbf{s}_0] \leftarrow$ design and slack variables
$r_{max} \leftarrow \max\{(\mathbf{x}_0 - \mathbf{x})^T(\mathbf{x}_0 - \mathbf{x}) : \mathbf{Ax} = \mathbf{b}, \mathbf{x} \geq 0\}$ {Maximum radius optimization (design variables only)}
$\mathcal{P} \leftarrow \{\mathbf{X}_0\}$ {Initialize population}
$f_{global} \leftarrow$ Evaluate($\mathbf{x}_0$), $\mathbf{x}^* \leftarrow \mathbf{x}_0$
for $g = 1$ to G **do**
  $\mathcal{C} \leftarrow \emptyset$ {New candidates}
  $n_{per\_survivor} \leftarrow \lfloor N_{gen}/|\mathcal{P}| \rfloor$
  $n_{remainder} \leftarrow N_{gen} \bmod |\mathcal{P}|$
  for each $\mathbf{p}_i \in \mathcal{P}$ **do**
    $n_{points} \leftarrow n_{per\_survivor} + \mathbf{1}_{i<n_{remainder}}$
    for $j = 1$ to n_{points} **do**
      $\mathbf{X}_{new} \leftarrow$ GenerateCandidate($\mathbf{A}$, $\mathbf{b}$, $\mathbf{p}_i$, g, K_{max}, r_{max})
      $\mathbf{x}_{new} \leftarrow$ extract design variables from $\mathbf{X}_{new}$
      $f_{new} \leftarrow$ Evaluate($\mathbf{x}_{new}$, $iteration$)
      $\mathcal{C} \leftarrow \mathcal{C} \cup \{(\mathbf{X}_{new}, f_{new})\}$
      if $f_{new} < f_{global}$ **then**
        $f_{global} \leftarrow f_{new}$, $\mathbf{x}^* \leftarrow \mathbf{x}_{new}$
      end if
    end for
  end for
  $\mathcal{A} \leftarrow \mathcal{P} \cup \mathcal{C}$ {Combine populations}
  Sort $\mathcal{A}$ by fitness values
  $\mathcal{P} \leftarrow$ RemoveRedundant($\mathcal{A}$, g, N_{pop}, r_{max})
end for
return $\mathbf{x}^*$, f_{global}

Algorithm 2 Generate Candidates

Require: Constraint matrix $\mathbf{A}$, bounds $\mathbf{b}$, parent $\mathbf{p}$, generation g, max pivots K_{max}, radius r_{max}
Ensure: New solution $\mathbf{X}_{new}$
$\phi^{-1} \leftarrow \frac{2}{1+\sqrt{5}}$
$\mathbf{x}_0 \leftarrow$ extract design variables from $\mathbf{p}$ {dimension n}
$\mathbf{s}_0 \leftarrow$ extract slack variables from $\mathbf{p}$ {dimension m}
$r_{target} \leftarrow (\phi^{-1})^g \cdot r_{max} \cdot$ Uniform$(0, 1)$
{Initialize groupings with updated slack variables}
for each group j **do**
  $\mathbf{x}_j \leftarrow \mathbf{p}[j]$ {Design variables for group j}
  $\mathbf{s}_{l,j} \leftarrow \mathbf{x}_j - \mathbf{b}_{lower}[j]$ {Lower slack variables}
  $\mathbf{s}_{u,j} \leftarrow \mathbf{b}_{upper}[j] - \mathbf{x}_j$ {Upper slack variables}
end for
$r_{current} \leftarrow 0$, $k \leftarrow 0$
while $k < K_{max}$ **and** $r_{current} < 0.95 \cdot r_{target}$ **do**
  Select random group j, direction $d \in \{-1, +1\}$, index i
  Backup current state: $\{\mathbf{x}_j^{(k)}, \mathbf{s}_{l,j}^{(k)}, \mathbf{s}_{u,j}^{(k)}\}$
  {Calculate maximum feasible pivot}
  if $d > 0$ **then**
    $U_{max} \leftarrow \min(\mathbf{s}_{u,j}[i], \min(\mathbf{s}_{l,j}[\neg i]) \cdot (|j| - 1))$
  else
    $U_{max} \leftarrow \min(\mathbf{s}_{l,j}[i], \min(\mathbf{s}_{u,j}[\neg i]) \cdot (|j| - 1))$
  end if
  $U \leftarrow d \cdot$ Uniform$(0, U_{max})$
  $\mathbf{x}_j[i] \leftarrow \mathbf{x}_j[i] + U$ {Update design variable}
  $\mathbf{x}_j[\neg i] \leftarrow \mathbf{x}_j[\neg i] - \frac{U}{|j|-1}$ {Update other design variables}
  Update corresponding slack variables $\mathbf{s}_{l,j}$ and $\mathbf{s}_{u,j}$
  $\mathbf{x}_{current} \leftarrow [\mathbf{x}_j]$ for all j {Current design variables only}
  $r_{new} \leftarrow \|\mathbf{x}_{current} - \mathbf{x}_0\|$ {Distance in design space only}
  if $r_{new} \leq r_{target}$ **then**
    $r_{current} \leftarrow r_{new}$
    if $r_{current} \geq 0.95 \cdot r_{target}$ **then**
      break {Early exit near target}
    end if
  else
    Restore: $\{\mathbf{x}_j, \mathbf{s}_{l,j}, \mathbf{s}_{u,j}\} \leftarrow \{\mathbf{x}_j^{(k)}, \mathbf{s}_{l,j}^{(k)}, \mathbf{s}_{u,j}^{(k)}\}$
  end if
  $k \leftarrow k + 1$
end while
return $[\mathbf{x}_{current}; \mathbf{s}_{l,j}; \mathbf{s}_{u,j}]$ for all j

[3] J. Suh, S. Homans, and M. Yim, "Telecubes: mechanical design of a module for self-reconfigurable robotics," in *Proceedings 2002 IEEE International Conference on Robotics and Automation (Cat. No.02CH37292)*, vol. 4, pp. 4095–4101 vol.4.

[4] S. Hossain, C. A. Nelson, and P. Dasgupta, "Rogensid: A rotary plate genderless single-sided docking mechanism for modular self-reconfigurable robots," in *International Design Engineering Technical Conferences and Computers and Information in Engineering Conference*, vol. 55942, p. V06BT07A011, American Society of Mechanical Engineers, 2013.

[5] Z. Guanghua, D. Zhicheng, and W. Wei, "Realization of a modular reconfigurable robot for rough terrain," in *2006 International Conference*

Algorithm 3 Redundancy Removal

Require: Sorted population $\mathcal{A}$, generation g, population size N_{pop}, radius r_{max}
Ensure: Filtered survivors $\mathcal{P}_{new}$

function RemoveRedundant($\mathcal{A}$, g, N_{pop}, r_{max})
  $\phi^{-1} \leftarrow \frac{2}{1+\sqrt{5}}$
  $r_{next} \leftarrow (\phi^{-1})^g \cdot r_{max}$
  $\mathcal{P}_{filtered} \leftarrow \emptyset$
  for each $(\mathbf{X}_i, f_i) \in \mathcal{A}$ **do**
    $redundant \leftarrow$ false
    for each $\mathbf{s} \in \mathcal{P}_{filtered}$ **do**
      $\mathbf{x}_i \leftarrow$ extract design variables from $\mathbf{X}_i$
      $\mathbf{x}_s \leftarrow$ extract design variables from $\mathbf{s}$
      if $\|\mathbf{x}_i - \mathbf{x}_s\|_2 < r_{next}$ **then**
                                                ▷ Distance in design space
        $redundant \leftarrow$ true
        break
      end if
    end for
    if not $redundant$ **and** $|\mathcal{P}_{filtered}| < N_{pop}$ **then**
      $\mathcal{P}_{filtered} \leftarrow \mathcal{P}_{filtered} \cup \{\mathbf{X}_i\}$
    end if
    if $|\mathcal{P}_{filtered}| = N_{pop}$ **then**
      break
    end if
  end for
  return $\mathcal{P}_{filtered}$

on Mechatronics and Automation, pp. 289–294. ISSN: 2152-744X.

[6] M. Yim, D. Duff, and K. Roufas, "PolyBot: a modular reconfigurable robot," in *Proceedings 2000 ICRA. Millennium Conference. IEEE International Conference on Robotics and Automation. Symposia Proceedings (Cat. No.00CH37065)*, vol. 1, pp. 514–520 vol.1. ISSN: 1050-4729.

[7] M. Nilsson, "Heavy-duty connectors for self-reconfiguring robots," in *Proceedings 2002 IEEE International Conference on Robotics and Automation (Cat. No.02CH37292)*, vol. 4, pp. 4071–4076 vol.4.

[8] G. Qiao, G. Song, J. Zhang, H. Sun, W. Wang, and A. Song, "Design of transmote: A modular self-reconfigurable robot with versatile transformation capabilities," in *2012 IEEE International Conference on Robotics and Biomimetics (ROBIO)*, pp. 1331–1336.

[9] F. Mondada, L. M. Gambardella, D. Floreano, S. Nolfi, J.-L. Deneuborg, and M. Dorigo, "The cooperation of swarm-bots: Physical interactions in collective robotics," *IEEE Robotics & Automation Magazine*, vol. 12, no. 2, pp. 21–28, 2005.

[10] W. Wang, W. Yu, and H. Zhang, "Jl-2: A mobile multi-robot system with docking and manipulating capabilities," *International Journal of Advanced Robotic Systems*, vol. 7, no. 1, p. 9, 2010.

[11] H. Wei, Y. Chen, J. Tan, and T. Wang, "Sambot: A self-assembly modular robot system," *IEEE/ASME transactions on mechatronics*, vol. 16, no. 4, pp. 745–757, 2010.

[12] A. Sproewitz, M. Asadpour, A. Billard, P. Dillenbourg, and A. Ijspeert, "Roombots–modular robots for adaptive furniture," in *IROS Workshop on Self-Reconfigurable Robots, Systems and Applications*, 2008.

[13] H. Kurokawa, K. Tomita, A. Kamimura, S. Kokaji, T. Hasuo, and S. Murata, "Distributed self-reconfiguration of m-tran iii modular robotic system," *The International Journal of Robotics Research*, vol. 27, no. 3-4, pp. 373–386, 2008.

[14] W. Saab and P. Ben-Tzvi, "Development of a novel coupling mechanism for modular self-reconfigurable mobile robots," in *International Design Engineering Technical Conferences and Computers and Information in Engineering Conference*, vol. 57137, p. V05BT08A007, American Society of Mechanical Engineers, 2015.

[15] E. H. Østergaard, K. Kassow, R. Beck, and H. H. Lund, "Design of the atron lattice-based self-reconfigurable robot," *Autonomous robots*, vol. 21, no. 2, pp. 165–183, 2006.

[16] C. Parrott, T. J. Dodd, and R. Groß, "HiGen: A high-speed genderless mechanical connection mechanism with single-sided disconnect for self-reconfigurable modular robots," in *2014 IEEE/RSJ International Conference on Intelligent Robots and Systems*, pp. 3926–3932. ISSN: 2153-0866.

[17] K. Torii, K. Uno, S. Santra, and K. Yoshida, "A sequential hermaphrodite coupling mechanism for lattice-based modular robots," in *2025 IEEE International Conference on Mechatronics (ICM)*, pp. 1–6. ISSN: 2837-1151.

[18] L. Zhao, Y. Jiang, M. Chen, K. Bekris, and D. Balkcom, "Modular shape-changing tensegrity-blocks enable self-assembling robotic structures," *Nature communications*, vol. 16, no. 1, p. 5888, 2025.

[19] S. Murata, E. Yoshida, A. Kamimura, H. Kurokawa, K. Tomita, and S. Kokaji, "M-TRAN: self-reconfigurable modular robotic system," vol. 7, no. 4, pp. 431–441.

[20] J. W. Romanishin, K. Gilpin, and D. Rus, "M-blocks: Momentum-driven, magnetic modular robots," in *2013 IEEE/RSJ International Conference on Intelligent Robots and Systems*, pp. 4288–4295. ISSN: 2153-0866.

[21] V. Zykov, E. Mytilinaios, M. Desnoyer, and H. Lipson, "Evolved and designed self-reproducing modular robotics," *IEEE Transactions on robotics*, vol. 23, no. 2, pp. 308–319, 2007.

[22] J. Davey, N. Kwok, and M. Yim, "Emulating self-reconfigurable robots - design of the SMORES system," in *2012 IEEE/RSJ International Conference on Intelligent Robots and Systems*, pp. 4464–4469. ISSN: 2153-0866.

[23] G. Fu, A. Menciassi, and P. Dario, "Development of a genderless and fail-safe connection system for autonomous modular robots," in *2011 IEEE International Conference on Robotics and Biomimetics*, pp. 877–882.

[24] B. Wang, W. Zhang, J. Luo, and Q. Xu, "Design of a modular wall-climbing robot with multi-plane transition and cleaning capabilities," *Biomimetics*, vol. 10, no. 7, p. 450, 2025.

[25] C. Liu, Q. Lin, H. Kim, and M. Yim, "Smores-ep, a modular robot with parallel self-assembly," *Autonomous Robots*, vol. 47, no. 2, pp. 211–228, 2023.

[26] Z. Yang, S. Zhao, K. Han, J. Qi, N. Zhao, X. Sui, J. Fan, J. Zhao, and Y. Zhu, "Design of a multi-environmentally adaptable modular self-reconfigurable robot," *IEEE Robotics and Automation Letters*, vol. 9, no. 10, pp. 8627–8634, 2024.

[27] Y. Zhang, T. Zheng, J. Fan, G. Li, Y. Zhu, and J. Zhao, "Nonlinear modeling and docking tests of a soft modular robot," *IEEE access*, vol. 7, pp. 11328–11337, 2018.

[28] A. Vergara, Y.-s. Lau, R.-F. Mendoza-Garcia, and J. C. Zagal, "Soft modular robotic cubes: toward replicating morphogenetic movements of the embryo," *PloS one*, vol. 12, no. 1, p. e0169179, 2017.

[29] J. Zou, Y. Lin, C. Ji, and H. Yang, "A reconfigurable omnidirectional soft robot based on caterpillar locomotion," vol. 5, no. 2, pp. 164–174.

[30] M. Malley, B. Haghighat, L. Houel, and R. Nagpal, "Eciton robotica: Design and algorithms for an adaptive self-assembling soft robot collective," in *2020 IEEE International Conference on Robotics and Automation (ICRA)*, pp. 4565–4571. ISSN: 2577-087X.

[31] Y. Zhang, Y. Li, D. Sui, L. Luan, T. Zheng, Z. Zhang, S. Zhao, F. Zhang, D. Li, and Y. Zhu, "Design and motion analysis of a soft modular robot for diverse environments," *Soft Robotics*, vol. 12, no. 5, pp. 662–675, 2025.

[32] L. Wang and F. Iida, "Towards "soft" self-reconfigurable robots," in *2012 4th IEEE RAS & EMBS International Conference on Biomedical Robotics and Biomechatronics (BioRob)*, pp. 593–598. ISSN: 2155-1782.

[33] B. Yang, A. M. Nasab, S. J. Woodman, E. Thomas, L. G. Tilton, M. Levin, and R. Kramer-Bottiglio, "Self-amputating and interfusing machines," *Advanced Materials*, vol. 36, no. 32, p. 2400241, 2024.

[34] J. Germann, M. Dommer, R. Pericet-Camara, and D. Floreano, "Active connection mechanism for soft modular robots," *Advanced Robotics*, vol. 26, no. 7, pp. 785–798, 2012.

[35] C. Freeman, J. Conzola, and V. Vikas, "Topology design and optimization of modular soft robots capable of homogenous and heterogenous reconfiguration," *Journal of Computational and Nonlinear Dynamics*, vol. 18, no. 6, p. 061007, 2023.

[36] R. Lakes and R. Witt, "Making and characterizing negative poisson's ratio materials," *International Journal of Mechanical Engineering Education*, vol. 30, no. 1, pp. 50–58, 2002.

[37] L. Marechal, P. Balland, L. Lindenroth, F. Petrou, C. Kontovounisios, and F. Bello, "Towards a common framework and database of materials for soft robotics," *Soft Robotics*, vol. 0, no. 0, p. null, 2020.